ORIGINAL ARTICLE

Additive manufacturing of Ti-6Al-4V alloy by micro-laser metal wire deposition with pulsed wave emission: processability and microstructure formation

Yunlong Fu[1,2,3] · Ali Gökhan Demir[2] 🔘 · Ning Guo[1,3]

Abstract

In this work, the micro-laser metal wire deposition (μLMWD) with ms-pulsed wave emission and low duty cycles was utilized to build the Ti-6Al-4V thin walls. The work first investigated the influence of the process parameters on single track stability and geometry. With the developed processing conditions thin walls with multiple layers were produced. The μLMWD produced thin walls were characterized by fine grain size expected to be due to the columnar to equiaxed transition (CET) in the produced wall. Fine columnar grains formed in the bottom region of wall due to the restriction of melt pool size and large cooling speed, while equiaxed grain formation and further refinement were achieved in the middle region, attributed to the intermittent stirring force that broke dendritic arms and increased nucleation events before solid–liquid interface. From the bottom to top region microstructures transferred from acicular α′ to short α lamella constituting basketweave structure, and the periodic heating and cooling generating by pulsed laser reduced the acicular α′ at higher cooling rate and decreased α size. The forming of equiaxed grain and fine grain and microstructure increased the wall microhardness.

Keywords Laser metal wire deposition · Pulsed wave emission · Ti-6Al-4V alloy · Grain refinement · Microstructure evolution · Microhardness

1 Introduction

Today a variety of additive manufacturing (AM) technologies employing different material feedstocks (e.g., powder or wire) and heat sources (e.g., arc, electron beam, laser) are adopted to fabricate complex, three-dimension and net-shaped metal components in the manufacturing industry [1–5]. There is, however, a trade-off between the dimensional resolution, deposition rate, material efficiency and requiring part size [6–9]. As vacuum atmosphere is not required and electromagnetic interference is absent, the laser AM (LAM), including laser directed energy deposition (LDED) and laser powder bed fusion (LPBF), has gained more attention as a stable and flexible technique for building high-accuracy components with complex geometry [10–13]. Compared to LPBF and powder-based laser metal deposition (LMD), the wire-based DED technique laser metal deposition (LMWD) avoids the powders recovery, provides higher building rate, less pollution and higher material use efficiency (up to 100%) [14–16]. Such advantages make the LMWD appealing [17–20] but the lower deposition precision resulting from large track dimension and asymmetric AM process restricts its further development [21, 22].

The Ti-6Al-4V alloy, a popular α (hexagonal close-packed structure, HCP) + β (body-centred cubic structure, BCC) titanium alloy, is extensively utilized in many fields such as aerospace, marine, aircraft structural, automobile and biomedical industries because of the excellent combination of mechanical property [13, 23]. A great quantity of researches into Ti-6Al-4V AM technologies in recent years have identified the necessity of preventing the formation of large columnar grains which could cause the anisotropy mechanical property and thus present challenges in building strategy and part design

✉ Ali Gökhan Demir
aligokhan.demir@polimi.it

1   State Key Laboratory of Advanced Welding and Joining, Harbin Institute of Technology, Harbin 150001, China

2   Department of Mechanical Engineering, Politecnico Di Milano, Via La Masa 1, 20156 Milan, Italy

3   Shandong Provincial Key Laboratory of Special Welding Technology, Harbin Institute of Technology at Weihai, Weihai 264209, China

[24]. Refining the grain size and promoting the columnar to equiaxed transition (CET) during AM are often perceived to be highly desirable. However, the lack of nuclei before the solid/liquid (S/L) interface and prevailing solidification conditions during AM process favour the epitaxial growth of grain and thus form the large columnar grains. In general, for wire arc additive manufacturing (WAAM) samples, the coarse columnar β grains could be observed clearly, in which the maximum width could be up to 0.7 mm while the length varied from 0.5 mm to 5 mm. In contrast, the samples built by LMD exhibited elongated columnar β grains of 0.1–0.3 mm width and 1–3 mm length [25]. Limited to the small molten pool size, the short columnar β grains with the average width of 150 μm and height of 200 μm formed during LPBF process [26]. A solution to achieve CET is to adjust the growth rate of the S/L interface (R) and temperature gradient (G). While the G/R decreased the CET during AM was promoted [27]. For example, after manipulating process parameters some equiaxed grains were observed in LPBF produced Ti-6Al-4V part though decreasing G [28]. Tan et al. [29] reported that a small amount of equiaxed grains formed on the top surface of deposited layer produced by LMD through increasing the laser power and applying synchronous induction assisted method to reduce the G/R ratio. As far as what has been published to date, it seemed almost impossible to achieve the full CET and significant grain refinement for AM produced Ti-6Al-4 V part only by changing the thermal conditions. Besides the G and R, the alloy constitution condition that drives nucleation events is another important factor in promoting CET and grain refinement. Bermingham et al. [24] reported that fine equiaxed grains with average grain size of 252 μm were obtained in WAAM with high linear energy density (LED) that was favourable on the basis of lower G/R ratio, after adding grain refining solute and nucleant particles. Xue et al. [30] demonstrated that the addition of boron powder into power-based LMD process of Ti-6Al-4V refined the prior β grains from 577 to 35 μm and the grain morphology changed to alternately short columnar and equiaxed from large columnar shape.

The microstructure transformation is another research focus for Ti-6Al-4V alloy AM because it plays a great role in the mechanical properties of deposited part, which mainly depends on the cooling rate at the β transus temperature (T_β) during the solidification process. Under the large heat input, e.g., WAAM and LMWD processes, the transformation microstructures of deposited metal include colony and basket-weave morphologies consisting of α lamella with a spacing of ~ 1 μm transferred from β by diffusion phase transition at lower cooling rate [31–33]. Yang et al. [34] stated that full acicular martensites α′ with different size scales formed within the LPBF produced part by the diffusionless transformation at high cooling rate far exceeding the critical value to produce martensite (~ 410 K/s) and resulting from a small heat input. Fu et al. [35] analyzed the microstructure

evolution mechanism in the LMWD fabricated Ti-6Al-4V walls, indicating that at the bottom region the microstructure was acicular α′ and with increasing the wall height the microstructure transferred into lamellar, lathy and blocky α phase gradually, attributed to different heat dissipation conditions. To this date, the control of grain size and shape of Ti-alloys remains an open point to be addressed in metal AM processes.

For LMWD of Ti-6Al-4 V alloy, solutions for improving the dimensional precision received less attention and the formation of large and columnar grains was often an undesirable but unavoidable result. A possible way to achieve smaller deposit tracks, while achieving a greater control of the cooling rates is through the use of long-pulsed laser sources. Such conditions have been explored in the literature concerning especially cladding and repair applications [36–38]. In the present study, the micro laser metal wire deposition (μLMWD) was firstly applied for the AM of Ti-6Al-4 V alloy. The μLMWD employs a long pulsed Nd:YAG laser source to deposit thin wires with diameters ≤ 0.5 mm. Conventional LMWD operates with wires diameters ≥ 1.0 mm enlarging the deposit size to several multiples of the wire diameter (3–5 mm). The long process allows the material to solidify between consecutive pulses, allowing to maintain a thinner deposit width similar to the wire diameter (0.6–1.0 mm). Hence, the obtained thin wall widths remain similar to the dimensional capability to LPBF [21, 39, 40]. Moreover, the processing conditions can allow to further enhance the grain and microstructure.

Accordingly, this work aims to study the influence of pulsed wave emission during the μLMWD of Ti-6Al-4V alloy in order to achieve thin-walled structures with refined grains. First, a fundamental study about the effect of process parameters on the single track geometry was provided, and the influence of height increment between neighboring layers over the wall formability was also investigated. At the most suitable deposition conditions, the thin-wall structures were built and the grain characteristic, microstructure transformation and microhardness at different regions of the thin wall were analyzed. Besides, a detailed description of the grain formation and microstructure transformation mechanisms was formulated through identifying the thermal conditions and analyzing the pulsed stirring process.

2 Experimental method

2.1 Experimental methods and sample characterization

The μLMWD was carried out utilizing a pulsed Nd:YAG laser source with Ti-6Al-4V wire of 0.5 mm diameter on a

Fig. 1 (**a**) diagram of the pulsed micro-wire laser metal deposition process; (**b**) photograph shows the experimental setup
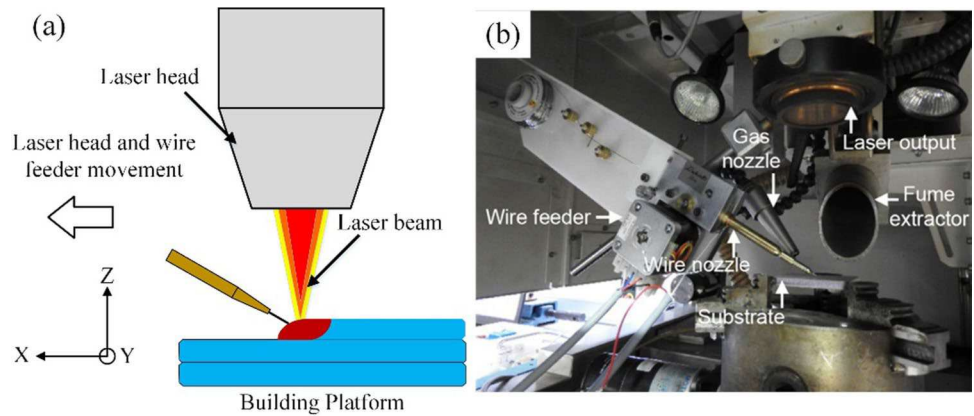
Table 1 Chemical compositions of the Ti-6Al-4 V alloy

Element	C	O	H	N	Al	V	Fe	Ti
wt.%	0.06	0.12	0.009	0.03	6.4	4.2	0.18	Bal

5-mm thickness Ti-6Al-4V substrate under the protection of a local argon shielding device. The diagram and specific photograph of the experimental device are displayed in Fig. 1 and the corresponding chemical compositions of Ti-6Al-4V alloy are listed in Table 1.

During the μLMWD process, the pulse repetition rate (PRR), wire feed rate (WFR), travel speed (v) and wire feeding angle (α) were fixed in order to allow a stable process after a preliminary study. The diameter of laser spot was set as 1.0 mm, 100% larger than the wire diameter, to achieve the full coverage for the wire at the high enough energy density. At the single-track experimental stage, the peak power (Ppk), pulse duration (τ) and gas flow rate of argon (G) changed adopting a 3^3 full factorial test plan to investigate the effect of Ppk, τ and G on the deposition appearance formability and determine the parameters producing smallest fusion depth and proper deposition width and height at stable deposition conditions. The statistical significance of the parameters was investigated applying analysis of variance (ANOVA), and the alpha value that controlled the statistical significance was set as 0.05. The specific process parameters are summarized in Table 2.

During μLMWD process, the choice of height increment between adjacent layers (Δz) is crucial to build three dimensional parts [39]. Multi-layer deposition walls with 10 layers at different Δz were executed using chosen parameter combinations that could provide stable and uniform single-track layer with small fusion depth and width, and the walls were analyzed to determine the most suitable Δz value allowing a stable process. After that, the single-bead wide walls with 80-layer height were built utilizing the same fixed parameters and the values of the varied parameters as identified in Table 3. The sample coordinate system is exhibited in Fig. 1, where X is the traveling direction of the laser source (TD), Z

Table 2 Process parameters in single track experimental phase

Fixed parameters		Level	
Spot diameter, d_s (mm)		1.0	
Pulse repetition rate, PRR (Hz)		7.0	
Wire feeding angle, α (°)		30	
Wire feeding direction		Front	
Wire feed rate, WFR (mm/min)		230	
Transverse speed, v (mm/min)		100	
Varied parameters	Levels		
	Low	Mid	High
Peak power, Ppk (kW)	0.8	1.1	1.4
Pulse duration, τ (ms)	7	8.2	9.4
Gas flow rate, G (L/min)	2	5	8

Table 3 The chosen process parameters in multi-layer deposition experiments

Fixed parameters	Level
Peak power, Ppk (kW)	0.9
Pulse duration, τ (ms)	7
Duty cycle, δ	4.9%
Point distance, d_p (μm)	238
Gas flow rate, G (L/min)	5

is the building direction normal to the deposited layer (ND) and Y is the horizontal direction (HD). During the μLMWD process the laser source released consecutive pulses with a fixed PRR and τ moving parallel to the wall length with a v. In the employed processing conditions the duty cycle (δ) was 4.9%, while the spatial distance between the consecutive irradiation zones (point distance, d_p) was 238 μm. All thin walls were produced via single tracks applied in the same direction, without an interlayer delay between the consecutive layers.

The time between consecutive layers was given by the time required to move the wire feeder to the starting point of the new layer, which corresponds to approximately 3 s.

The preparation of metallographic specimens was performed on the cross sections of deposited wall cut firstly perpendicular to the TD, then grinded by abrasive grinding papers with decreasing coarseness to 2000 grit and finally polished by polishing agent with the gradually decreasing size from 6 to 1 μm. After etching by the Kroll's agent, macrostructures on cross sections were captured by optical microscopy (Leitz Ergolux 200 from Leica, Wetzlar, Germany), and the microstructures of metallographic specimens from different regions of the wall were obtained using SEM (LEO 1413 from Zeiss, Oberocken, Germany). Electron Back Scatter Diffraction (EBSD) was also carried out on the cross sections to further study the morphology of α/α′ and investigate the phase composition, "grain" size and misorientation distribution using with step sizes from 0.2 to 1.6 mm and 20 kV accelerating voltage. Finally, the Vickers microhardness of multi-layer thin wall on cross sections with an interval of 0.1 mm were measured by a hardness tester utilizing a 100-g load for 15 s.

2.2 Thermal conditions in μLMWD

In this work, a solidification map, which could predict the solidification mode of Ti-6Al-4V by the G and R, from the seminal empirical work developed by Kobryn and Semiatin [41] was used to helpfully investigate the grain formation mechanism under the thermal environment in μLMWD. Besides, the thermal history, especially the cooling rate at T_β, during μLMWD is another important factor playing a great role in the microstructure transformation process. During μLMWD, the accurate measurement of G and R across the molten pool and the thermal history by experiment method is almost impossible because of the high temperature in excess of melting or even boiling point and small molten pool size. Thus, a numerical simulation was performed to simulate the temperature field of μLMWD and obtain the thermal history, G and R to discuss the grain formation and microstructure transformation mechanisms.

The governing equation of the nonlinear transient heat transfer was given by

$$\frac{\partial}{\partial x}\left[k_x(T)\frac{\partial T}{\partial x}\right] + \frac{\partial}{\partial y}\left[k_y(T)\frac{\partial T}{\partial y}\right] + \frac{\partial}{\partial y}\left[k_z(T)\frac{\partial T}{\partial z}\right] + q = \rho(T)C(T)\frac{\partial T}{\partial t} \tag{1}$$

where T was the temperature, ρ was the temperature-dependent density, C was the specific heat capacity, q was the applied heat generation source, and k was the thermal conductivity.

During the laser pulse duration, the heat generation rate q was defined by the Gauss volumetric conical heat source [38] that could be expressed by

$$q(r) = \frac{9\eta P}{\pi H(1 - e^{-3})(r_e^2 + r_e r_i + r_i^2)}\exp\left(-\frac{3r^2}{r_H^2}\right) \tag{2}$$

where η was the efficiency coefficient, P was the laser power, the r was the distance between node and laser beam center and r_H was the heat distribution coefficient which could be given by

$$r_H(z) = r_i + \left(r_e - r_i\right)\frac{z - z_i}{z_e - z_i}. \tag{3}$$

where r_e and r_i were the maximum and minimum radiuses of the laser beam in the conical heat source respectively, and z_e and z_i were the corresponding coordinate of the r_e and r_i in the Z-axis. H was the distance between z_e and z_i.

The environment and initial temperatures were set to 25℃. In this model, the dimensions of the baseplate were 40 mm × 10 mm × 2.4 mm while those of the deposited metal were 1.2 mm × 10 mm × 28.8 mm, and the entire model was meshed by the thermal conduction element SOLID70. The convective heat transfers and thermal radiation losses were considered for the heat exchange between outer surfaces in the model and the environment, and the boundary conditions could be given by Eq. (4).

$$k_n(T)\frac{\partial T}{\partial n} + q_s + h_c\left(T - T_\infty\right) + \varepsilon\sigma\left(T^4 - T_\infty^{\ 4}\right) = 0 \tag{4}$$

where k_n was the thermal conductivity perpendicular to the surface boundary, q_s was the boundary heat flux, hc was the convective heat transfer coefficient, T_∞ represented the environment temperature, σ and ε were the Stefan-Boltzmann constant and the emissivity respectively. A commercial FEM software (ANSYS) was used for the calculations using birth and death method to simulate the wire deposition process, and the time step was 7 ms. The Newton–Raphson method was used to solve the model, which was calibrated by predictor–corrector method. The model was validated by means of micrographic analysis measuring the track size. The typical thermo-physical properties of Ti-6Al-4V are list in Table 4 and model parameters were set according to process parameters as displayed in Table 3. The detailed model description and properties at various temperatures could be found in [42–44].

3 Results and discussion

3.1 Formability characteristic

3.1.1 Single track

Figure 2 displays the deposited appearance of single tracks with the G of 2 L/min at different Ppk and τ. Almost all tracks were continuous and uniform, and exhibited silvery

Table 4 Thermo-physical properties of Ti-6Al-4 V titanium alloy

Thermal-physical property	Ti-6Al-4 V
Solidus temperature, (K)	1878
Liquidus temperature, (K)	1928
Evaporation temperature, (K)	3133
Density of solid metal, (kg/m³)	4420
Density of liquid metal, (kg/m³)	4000
Molar mass, (g/mol)	446.07
Specific heat of solid metal, (J/(kg•K))	670
Specific heat of liquid metal, (J/(kg•K))	730
Thermal conductivity at environment temperature, (W/(m•K))	7
Thermal conductivity at Liquidus temperature, (W/(m•K))	28.4
Enthalpy of solid at melting point, (J/kg)	1.12×10^6
Enthalpy of liquid at melting point, (J/kg)	1.49×10^6
Enthalpy change of evaporation, (J/kg)	4.7×10^6
Boltzmann's constant, (J/K)	1.38×10^{-24}

color, indicating the excellent protection effect was achieved during μLMWD process. In addition, the similar single tracks were obtained at 5 and 8 L/min gas flow rates. Figure 3 exhibits the cross sections of deposited single tracks positioned in the parameter space of the 3^3 full factorial test plan. The width of the tracks and penetration into base metal fluctuated in a large scale, which were minimal in condition with low Ppk and τ. With increasing the Ppk and τ, the μLMWD process transferred from conduction mode to conduction to keyhole transition mode. At low Ppk and τ, undercut defects were observed and the metallurgical bond between deposited metal and substrate was not reliable because of the insufficient laser energy.

The penetration depth (D), width (W) and deposit height (H) of single tracks were measured on cross sections. The D and W increased obviously with increasing the Ppk and τ, while no relationship between H and process parameters was observed. In order to analyze the D and W comprehensively, the fitted regression models were built. For the D, the regression model consisted of first order terms of Ppk

Fig. 2 Appearances of single tracks with 2 L/min gas flow rate at different peak powers and pulse durations: (**a**) 0.8 kW, 7 ms; (**b**) 0.8 kW, 8.2 ms; (**c**) 0.8 kW, 9.4 ms; (**d**) 1.1 kW, 7 ms; (**e**) 1.1 kW, 8.2 ms; (**f**) 1.1 kW, 9.7 ms; (**g**) 1.4 kW, 7 ms; (**h**) 1.4 kW, 8.2 ms; (**i**) 1.4 kW, 9.4 ms

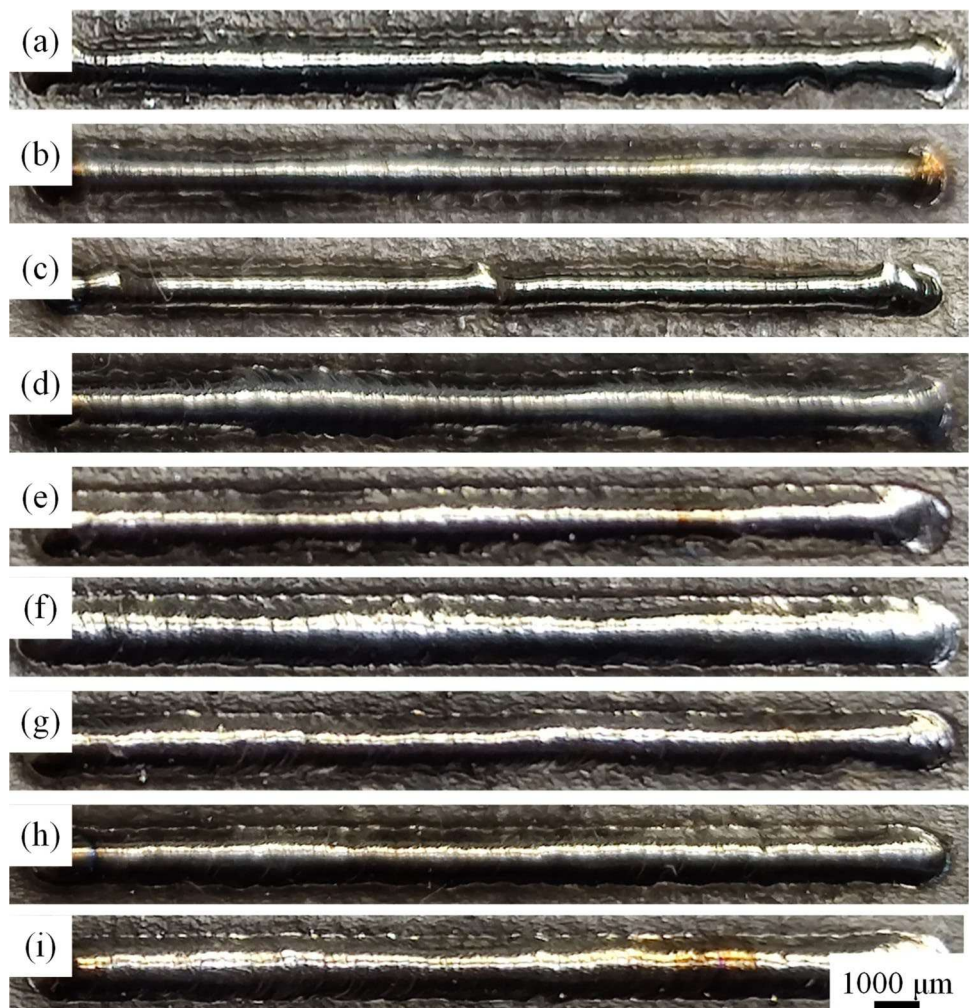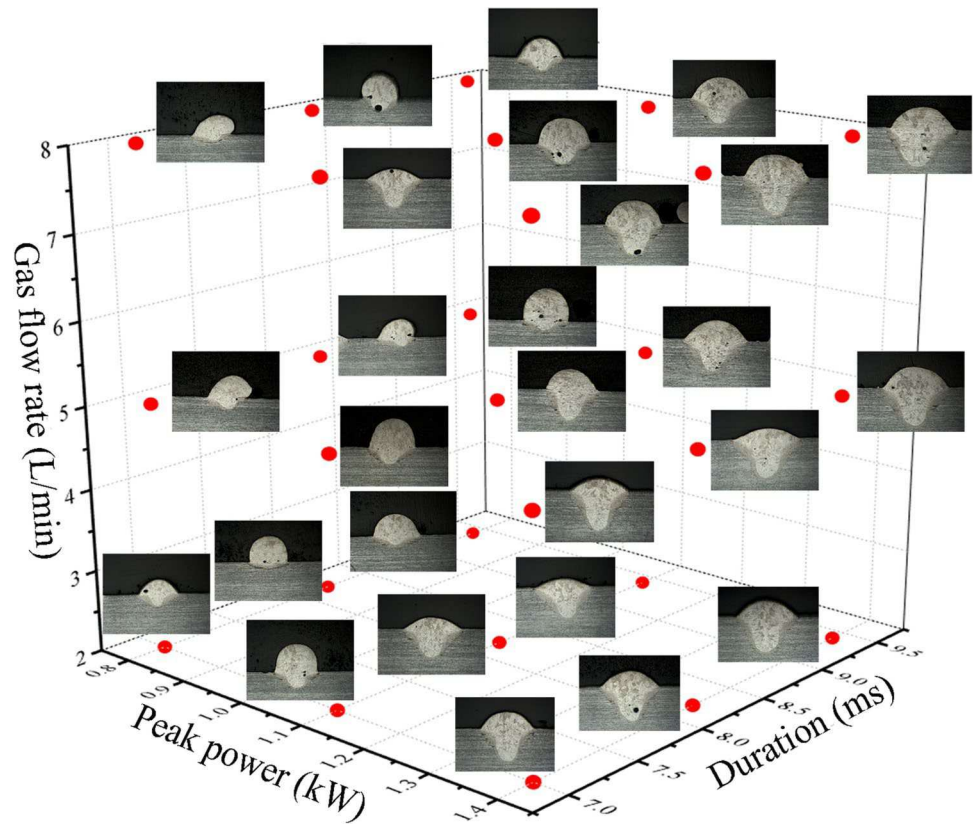**Fig. 3** Cross-sections of single tracks positioned in the parameter space of the 3^3 full factorial test plan

and τ and second order of τ, which could be written as the following equation.

$$D(\mu m) = 990.6 \times Ppk - 164.74 \times t + 12.74 \times t^2 \quad (5)$$

This model fitted the data well with R^2_{adj} at 96.45%. Figure 4 shows the corresponding contour plot. The penetration depth varied in a large range exceeding 600 μm, and the effect of Ppk on penetration depth was more significant compared with that of τ. During μLMWD process, the higher Ppk increased the laser energy density irritated on the substrate directly, which promoted the melting and evaporation of base metal and hence increased the penetration depth significantly. For square shaped laser pulses, the pulse laser energy (E) is equal to the product of Ppk and τ. The larger τ increased the E within a whole pulse period and promoted the heat transfer inside the molten pool, giving rise to the larger penetration depth.

The W regression model consisted of first order term of Ppk and second order terms as expressed in the following equation.

$$W(\mu m) = 1175.6 \times Ppk - 421.1 \times Ppk^2 + 59.45 \times Ppk \times t \quad (6)$$

This model fitted the data adequately with R^2_{adj} at 99.54%. The contour plot of this regression model is reported in

Fig. 4, indicating the W changed between 1100 μm and 1600 μm. Similar to H, the Ppk influenced the variety of W more obviously.

For building multi-layer walls, the sufficient laser energy is required to avoid defects such as undercut and incomplete fusion and obtain reliable metallurgical bonds between layers. However, the high laser energy would generate excessive heat accumulation and the resultant large penetration depth could increase the thermal cycles that the deposited metal experienced. From these points of view, limited amounts of width (1000–1100 μm) and depth (350–450 μm) were suggested to provide stable deposition condition with width and depth values as small as possible. Based on the regression models, the contour plot of width and depth with limited values was drawn, as shown in Fig. 5. The Ppk and τ were set at 0.9 kW and 7 ms respectively in the thin-walled structure manufacturing stage.

3.1.2 Multi-layer deposition

A common problem in directed energy deposition processes, namely the mismatch between height increment (Δz) and effective layer height (H), also manifests in μLMWD. The 10-layer walls with different height increments at optimized process parameters were built, whose surface appearances are shown in Fig. 6, and the effect of
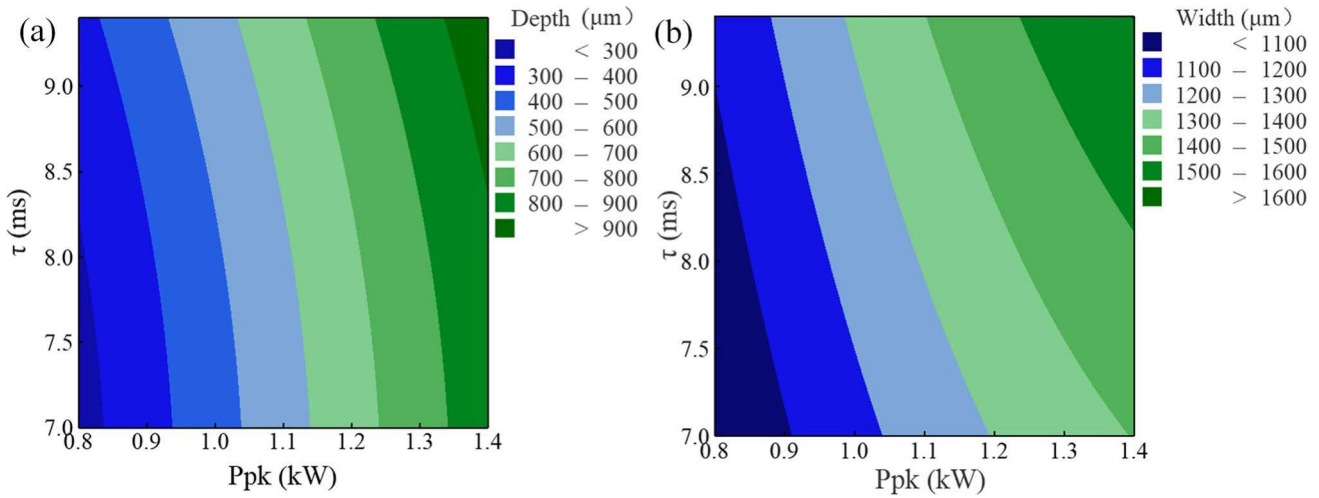
Fig. 4 Contour plot of penetration depth and width as a function of Ppk and τ: (**a**) penetration depth; (**b**) width
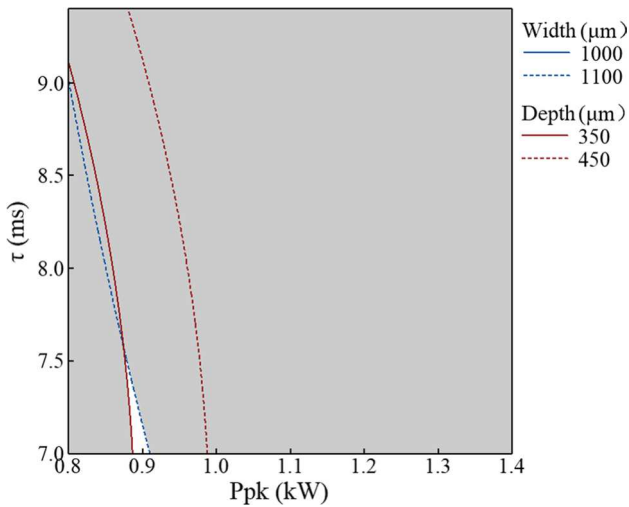

Fig. 5 The contour plot of width and depth with limited values

height increment on the wall surface roughness is depicted in Fig. 7. While the surface roughness measurements are indicative of the surface micro-scale roughness macroscopic defects related to the influence of height increment are visible. Too low values of Δz at 0.28–0.32 mm appear to generate track instabilities. Conversely at high levels of Δz at 0.44 mm track deviations appear presumably due to stubbing related defects. In all multi-layer deposition conditions heat accumulation was observed visibly through the end of the deposition as the thin-walls remained incandescently glowing after the turning-off of the laser source. Such conditions did not occur throughout the single-layer depositions.

At the 0.28 mm Δz, the height increment was lower than effective layer height ($\Delta z < H$), and with increasing

the deposited layer the wire stability reduced gradually as the solid wire could not be melted immediately by laser and even impact the deposited metal violently, generating the poor deposition formability and resulting in the ununiform wall appearance with high surface roughness, as shown in Figs. 6(a) and 7. With the increase of Δz from 0.28 to 0.36, the wall appearance improved and the surface roughness reduced gradually, because the mismatch between Δz and H disappeared. In conditions where the height increment was greater than effective layer height ($\Delta z > H$) the wire was above the deposited metal region that the laser beam irradiated, and thus large metal droplet formed before transferring into the molten pool and even wire detachment occurred, giving rise to the intermittent μLMWD process. Consequently, while the Δz exceeded 0.36 mm, the bulges between neighboring layers were obvious and the surface roughness of walls increased continuously with the increase of Δz as shown in Figs. 6 and 7. In order to obtain stable condition without a mismatch between the Δz and H, the Δz was fixed at 0.36 mm in the following multi-layer wall manufacturing process.

3.2 Grain structure

3.2.1 Grain characteristics

The single-bead wide walls with 80-layer height were built utilizing the optimized process parameters and height increment, whose grain formation, microstructure transformation and microhardness were investigated. Figure 8 shows the macrostructures captured by optical microscope and measured grain size in different regions of the wall deposited by μLMWD. It could be observed from Fig. 8(a) that the bottom region of sample contained
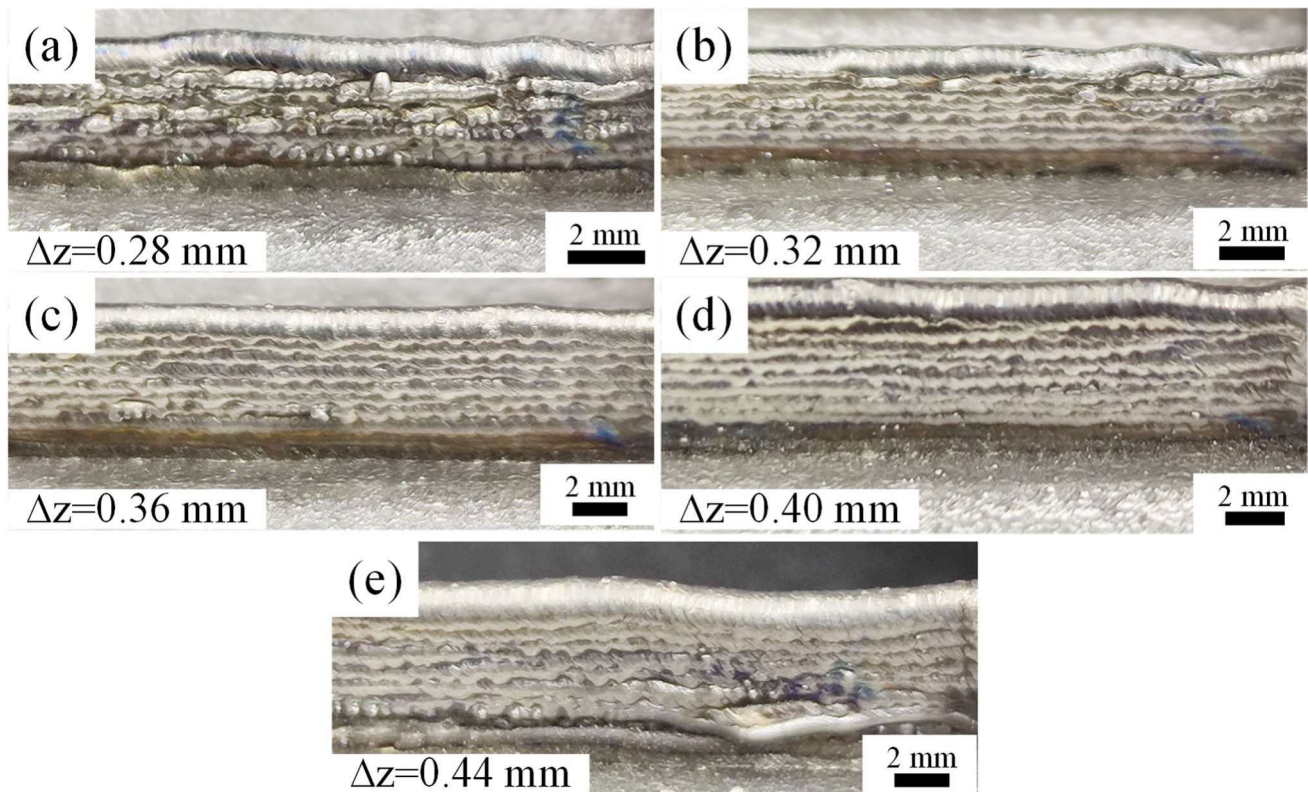
Fig. 6 Surface appearances of 10-layer deposited thin walls with **a**) $\Delta z = 0.28$ mm, **b**) $\Delta z = 0.32$ mm, **c**) $\Delta z = 0.36$ mm, **d**) $\Delta z = 0.40$ mm, **e**) $\Delta z = 0.44$ mm
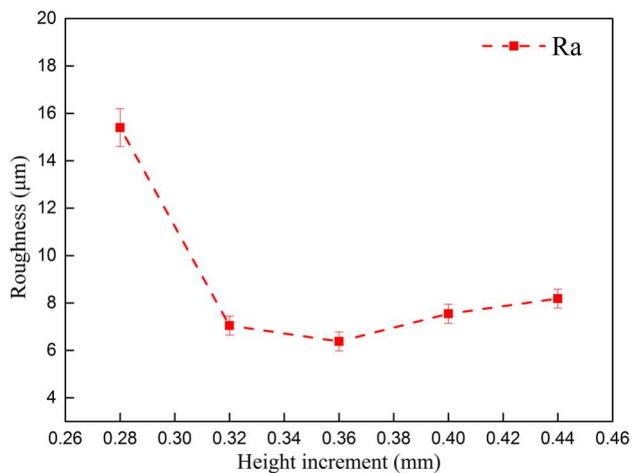

Fig. 7 Surface roughness of walls with different height increments. Error bars indicate standard deviation

mostly columnar grains, and at the 1st and 2nd layers the grain size ranged from 100 to 1416 μm in length and from 25 to 240 μm in width. The grains were larger in the successive layers of the bottom region. Almost in all AM manufactured Ti-6Al-4 V components, the large columnar prior-β grains, extending over multi layers formed owing

to a shortage of nucleation sites near the S/L interface and the solidification conditions favouring the epitaxial growth of grains from base metal or previously deposited layers because of similarities in the surface energy and composition of the metal. The size of columnar β grain was closely associated with the heat source. As reported in the literature concerning the same alloy, in the WAAM produced parts, the width of columnar grain was 0.7 mm and the length reached 5 mm, while those in LMD produced parts width could be up to 0.3 mm and length up to 3 mm [25, 44]. Similarly to what was observed in the LMD and LMWD manufactured samples, the μLMWD process with long pulses and thin wire applied in this work failed to promote the CET in the bottom region of deposited metal, but it refined the grain size substantially.

As displayed in Fig. 8(b), the application of μLMWD process with the conditions given in this work succeeded in preventing the formation of columnar grain in the middle region where fine equiaxed grains formed with 45 μm diameter. The equiaxed grains were accompanied by short columnar β grains of 62 μm average width and 114 μm average length, which were found to be finer than those in LPBF manufactured samples [26]. The equiaxed grain size was about only a quarter of that in top region of LMWD wall and less than one fifth of that in WAAM wall that produced through
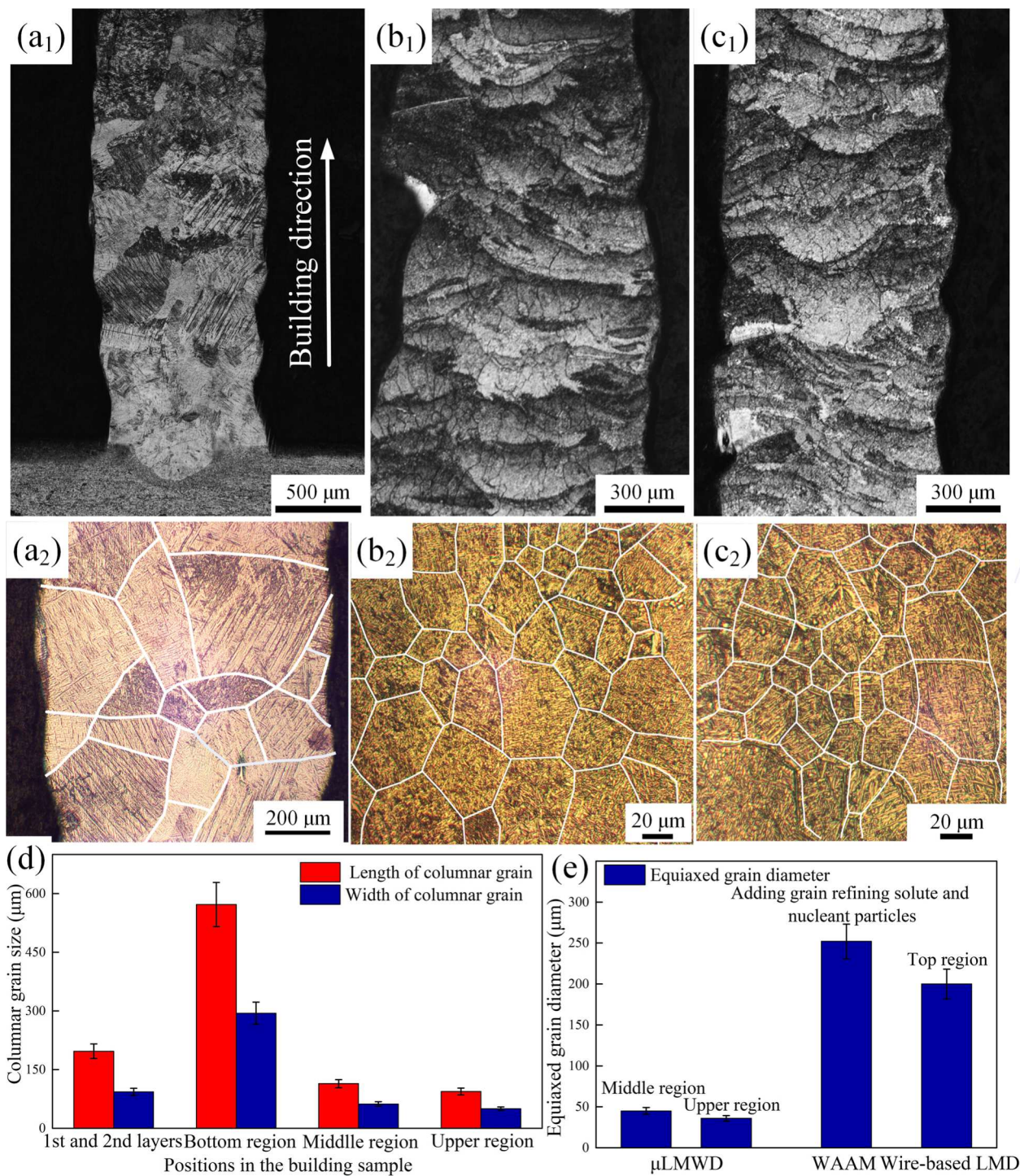
Fig. 8 Microstructures of the μLMWD wall: (**a**) bottom region; (**b**) middle region; (**c**) upper region; (**d**) average size of columnar grains; (**e**) average diameter of equiaxed grain forming in middle and upper regions μLMWD wall, WAAM wall produced through applying grain refining solute and nucleant particles and top region of wire-based LMD wall [24, 35]

applying nucleant particles and grain refining solute, as displayed in Fig. 8(e). This was a significant refinement and great change in grain morphology compared with grains in bottom region of μLMWD build and walls manufactured by

other additive manufacturing methods. In the upper region, the proportion of equiaxed grains increased, and the diameter of equiaxed grain reduced to 36 μm while the average width and length of columnar grain decreased to 50 μm and

94 μm respectively, indicating that the CET and the grain refinement were further promoted at successive layers.

3.2.2 Grain refinement and CET mechanism

Under the identical alloy constitution, the R, G and molten pool size are undeniably important factors determining the grain morphology and size during the grain formation and growth process. Kobryn and Semiatin [41] developed a solidification map to deduce the grain formation mode through the R and G, which was widely referenced in the AM field of Ti-6Al-4V and displayed in Fig. 9(d) to discuss the transition mechanism from columnar to equiaxed grain for the conditions studied here. For comparison the solidification condition of WAAM at the same deposition speed studied by Bermingham et al. [24] and the typical operating range for laser-based AM calculated by Bontha et al. [45] were also provided.

Under conventional WAAM processing conditions, a small G/R ratio at low thermal gradient, a slow cooling rate and a large melt pool were generated due to the higher LED, making it possible to generate only a small amount equiaxed grains. Bermingham et al. [24] reported that at LED = 1.49 kJ/mm for WAAM the low average thermal

gradient generated some equiaxed grains, while the grains were still mostly columnar. The diameter of equiaxed grain reached 1.5 mm three times larger than those in castings. Compared to WAAM, the LMWD possesses a higher cooling rate owing to lower LED. Hence, LMWD can potentially form thinner columnar grains but generating equiaxed grains is expected to be more difficult because of the high G/R ratio.

In this study the pulsed Nd:YAG laser source was applied during μLMWD process with a LED = 0.027 kJ/mm, much lower compared to WAAM and LMWD. Although this was unfavourable in terms of larger thermal gradient produced by lower LED that hindered the CET, the desirable consequence was obtained that a large amount of equiaxed grains formed in the middle and upper region of the μLMWD processed wall. Interestingly, the morphology and size of grains displayed and analysed in Fig. 8 demonstrated both the columnar and equiaxed grains were refined compared to WAAM and LMWD processes. As a general rule, the R could be approximated by the deposition speed, and the G would increase with decreasing the LED. With that in mind, the position of μLMWD in the solidification map should be located above that of WAAM and predict the full columnar grain morphology, inconsistent with the results. The thermal
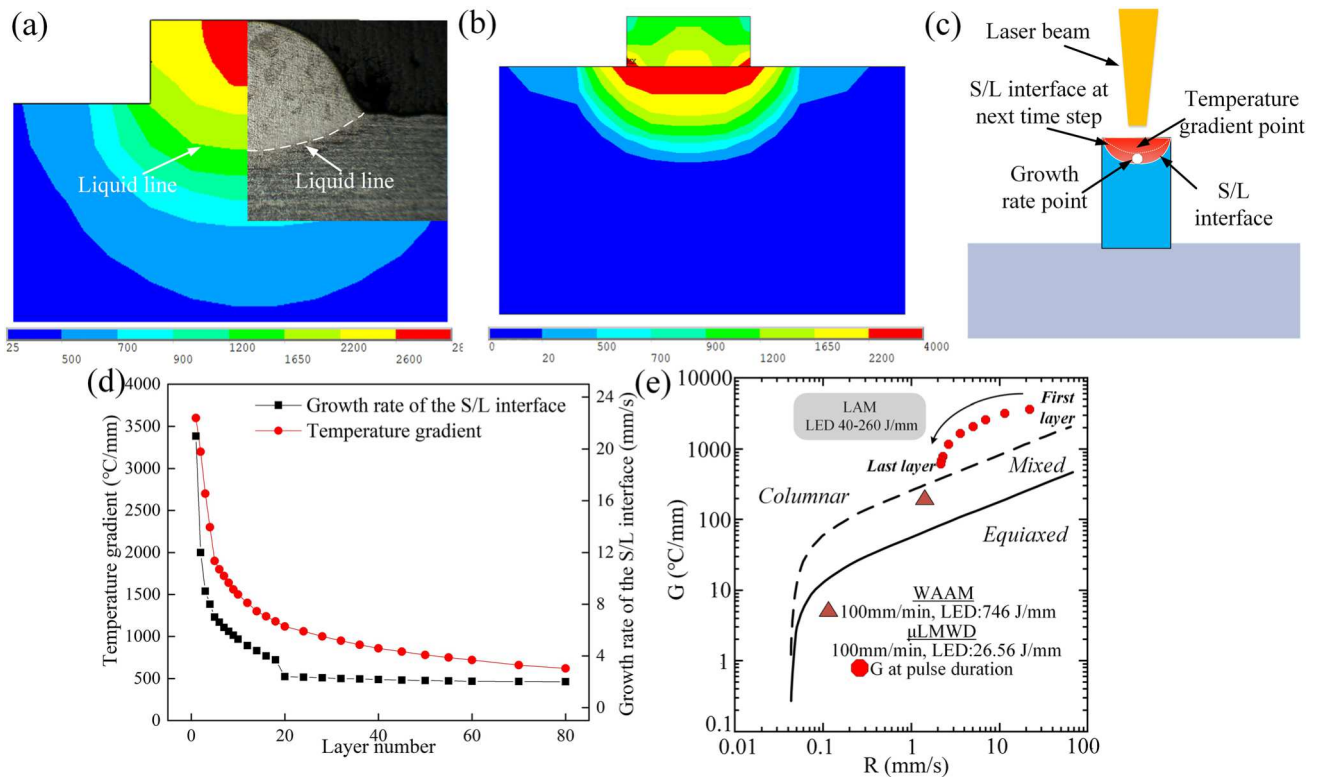

Fig. 9 Temperature, G and R during μLMWD obtained by numerical simulation: (**a**) temperature contour of the initial stage versus the cross section; (**c**) the position of the temperature gradient and the growth rate, which is in the center point between the solidus and liquidus on the cross-section of the wall; (**d**) G contour of the initial stage; (**e**) G and R during μLMWD; (**d**) Ti-6Al-4V solidification map [41] and a comparison to the WAAM and LAM are also provided [24, 45]

process during μLMWD, therefore, was investigated to analyse the grain formation mechanism in this paper.

The temperature contour of the initial stage during μLMWD versus the cross section of single track deposited under the same process parameters is exhibited in Fig. 9(a), indicating the numerical temperature contour had a good correspondence with the phase transformation region displayed on the micrograph. Figure 9(b–e) shows the G and R throughout the deposited metal, and the thermal cycles and crucial cooling rates at β transus temperature ($T_β$) in the centre of the track of different layers are also exhibited in Fig. 10. During the initial μLMWD process, the substrate and deposited metal were repeatedly irradiated by pulsed laser, and the molten metal generated by a single pulse had enough time to solidify before the arrival of the consecutive pulse in time, as demonstrated by the thermal cycle in Fig. 10(a). Given the periodic melting and solidifying process, the R of pulsed laser μLMWD far outweighed the deposition speed, different from the AM process with continuous heat input. The average G across the whole melt pool was approximately 1700 ℃/mm calculated by the temperature variation and the molten pool depth. Near the S/L interface the G reached 3600 ℃/mm, higher than average value, as shown in Fig. 9(b), which was found to remain the same

also with different pulse durations. Meanwhile, the R during the first layer was approximately 21 mm/s, which was determined by measuring the moving distance of S/L interface at neighbouring time steps. The average G and R on the cross section of the different deposited layers in the wall were calculated and the specific points in the pool were shown in Fig. 9(c) while the values were shown in Fig. 9(d). The G and R in solidification map predicted the columnar grain morphology during deposition at the first layer. The G and R during μLMWD were determined and plotted as a function of the deposited layer number for exploring the grain formation mechanism. The results indicated the steep temperature gradient within the high-temperature metal before S/L interface decreased rapidly as exhibited in Fig. 9(d). By contrast the R reduced sharply at the initial stage of μLMWD process and then a sharp decline occurred at the 20th layer because the molten pool would not solidify within the cooling process between two pulse durations due to the accumulation of heat in the built part as demonstrated in Fig. 10(c). In the solidification map, the G and R gradually approached the mixed columnar + equiaxed growth region, providing a condition that the formation of some equiaxed grains was possible because of the decrease of G/R ratio, as shown in Fig. 9(e).
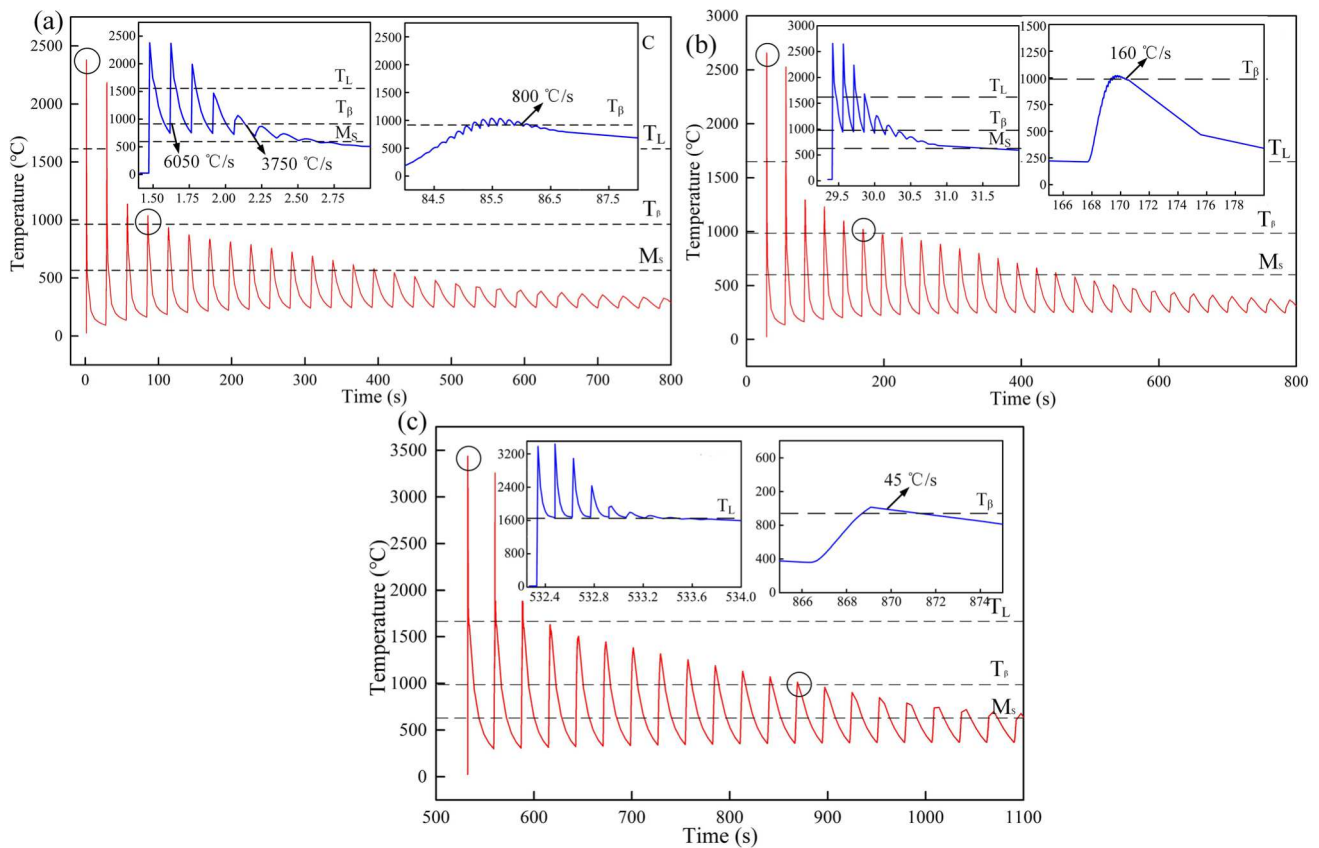

Fig. 10 Thermal cycles at different layers of building wall: (**a**) 1st layer; (**b**) 3rd layer; (**c**) 30th layer

The principle of the grain formation and growth model applied at different stages during μLMWD process is illustrated in Fig. 11. At the first layer, the primary dendrites formed inside molten pool under a steep thermal gradient in which no solute diffusion into liquid and constitutional supercooling occurred. Grains grew epitaxially along the building direction due to the strongly directed heat flux during solidification process, forming columnar grains similar to conclusions having been reported in [1, 45, 46]. According to [47, 48], the prior β grains grew competitively i.e. grains with easy-growth direction<100>parallel to maximum temperature gradient could preferentially grow instead of others, causing the growth direction of grains aligned with the $<100>_\beta$//Nz. At subsequent layers the partially-remelted columnar grains became nuclei and then the epitaxial regrowth was ongoing via re-melting and re-solidify processes, producing long grains extending over multi layers. The arm spacing λ of primary dendrite that characterize the columnar grain width also depends on the G and R [49], which could be expressed as

$$\lambda = aG^{-1/2}R^{-1/4} \tag{7}$$

where a is the coefficient related to material properties. The large G value during μLMWD solidification process

compared to that in the WAAM and LMWD refined the columnar grains whose growth was also restricted by the small molten pool size resulting from the low LED and applying of micro wire. The heat accumulation decreased the G gradually during the μLMWD process. At the bottom region above the 1st and 2nd layers of the built sample the G was still too steep to permit the equiaxed grain but the decrease of G and cooling rate gave rise to the coarsening of columnar grains. The second scenario was that the number of grains decreased with increasing the built height as the growth of unfavourably oriented tips was hindered through the competitive grain growth [14, 50].

Recalling the macrostructure in Fig. 8, the equiaxed grains with small diameter gradually took the place of columnar grains in the middle region and even the remainder columnar grains were refined significantly. The question was why so many equiaxed grains formed and the average grain size was much smaller compared to grains that formed in WAAM and LMWD processes in which although the segregating solute and nucleant particles were applied. The first reason was that the gradually reducing temperature gradient resulting from the heat accumulation provided the thermal

Fig. 11 The illustration diagram of grain formation and growth model during μLMWD: (**a**) columnar grain; (**b**) equiaxed grain. For the t_1-t_4 time stamps refer to text for a detailed description of the event sequence
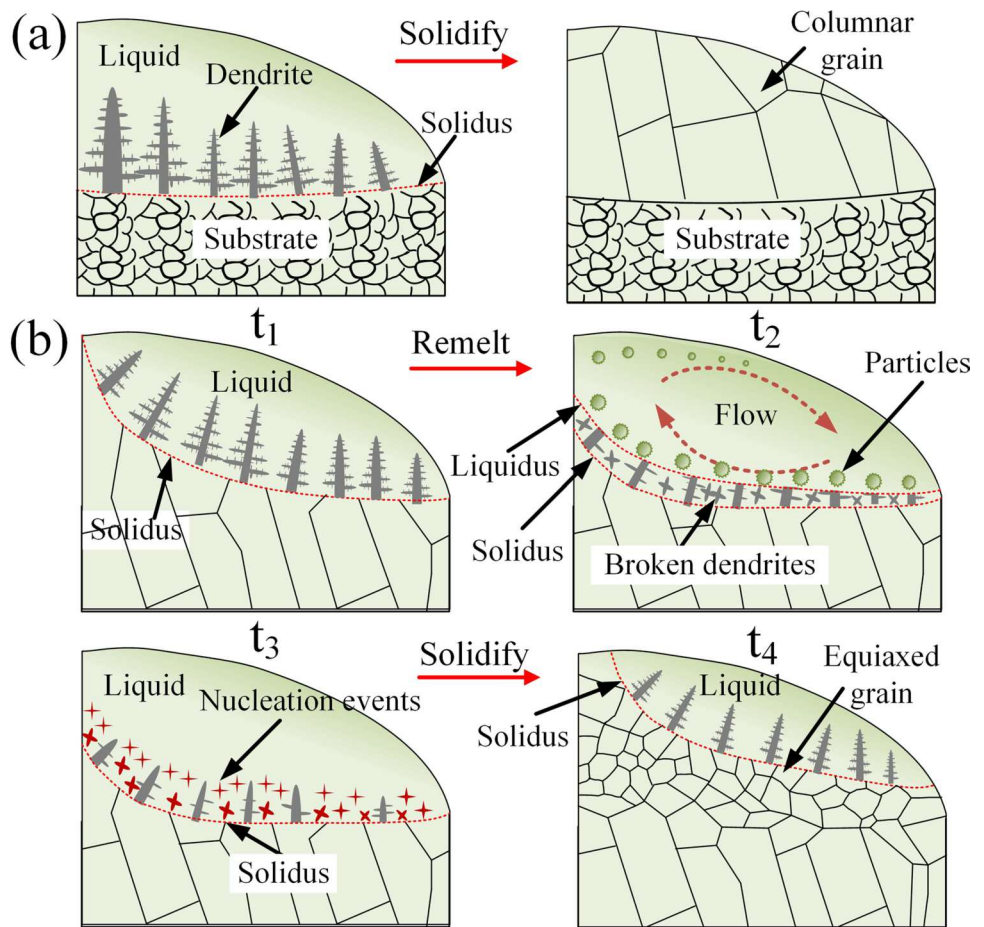
condition at the middle and upper region of the building sample that was yet ready for nucleation. However, even in the middle region the average G across the whole melt pool was about 1000 ℃/mm, higher than that experienced in WAAM process which was in the order of 100 ℃/mm and mainly produced columnar grains [24]. Albeit the R value was also large, the μLMWD processes should form most coarse columnar grains rather than fine equiaxed grains. Considering that the equiaxed grains indeed formed, the most probable scenarios were discussed below.

Due to the existence of temperature gradient, the Marangoni force was activated during μLMWD, causing the rapid flow and thermal mixing of the molten metal within the melt pool, and the melt pool and thermal mixing only continue while the laser pulse was emitted [51, 52]. At the initial stage of μLMWD, the molten metal would solidify rapidly as long as the laser pulse passed owing to high cooling rate and the pool could equilibrate before complete solidification, as shown in Fig. 11(a). However, in the middle region of the sample the molten pool would persist (t_1) during the interval time between two neighbouring pulses as the cooling rate decreases, and the stirring force came back towards the un-solidified fluid (t_2) at the subsequent laser pulse duration. As illustrated in Fig. 11(b), under the action of stirring force the dendritic arms before the solidification interface fractured and then were transferred within the molten pool. Once the laser pulse passed, the broken dendritic arms were scattered in the whole pool. The dendritic arms in the high-temperature zone that was away from S/L interface would be melted, however, those dendritic arms located in the mushy zone where the temperature was between the T_L and T_S would continue to survive even when partially melted, and then formed solid particles (t_3). These incompletely melted broken dendrites continue to grow as crystal nuclei during subsequent solidification. On the other hand, the lower temperature gradient in the middle region expanded the mushy zone, meaning more nucleation particles were produced within the pool. Based on classical nucleation theory, only while the nuclei embryos reached a critical size (r*), the free grain growth could occur overcoming the interfacial energy barrier. The nucleation particles distributing within the pool allow molten metal to touch a larger surface and generate hemispherical caps, which significantly increases the nuclei curvature radius above r* and facilitates their growth, according to the Free Growth theory [53, 54]. Therefore, the broken dendritic arms that did not fully solidify acted as nucleation particles in the mushy zone and thus the nucleation could occur near a suitable particle, forming the equiaxed grains in the middle region of building (t_4). After this cooling duration, another laser pulse would stir the pool again and trigger subsequent equiaxed nucleation events, as exhibited in Fig. 11(b). As the μLMWD progressed, the decrease of G and R expanded the mushy zone further,

increasing the amount of equiaxed grains and further refining the grain in upper region.

3.3 Microstructure

3.3.1 SEM and EBSD

The microstructural distributions in distinctive regions of the 80-layer wall were investigated by SEM, and the EBSD analysis was used to quantitatively analyse the phase composition as well as α/α′ shape, size and grain boundary. Figure 12 exhibits the microstructure morphology in the bottom region of wall and the corresponding EDSD results. The EBSD phase map displayed in Fig. 12(e) and analysed in Fig. 12(f) suggests the bottom region of μLMWD produced Ti-6Al-4 V wall was composed basically of α/α′ phase (HCP structure) with 7% β phase (BCC structure) distributed in a dispersed way.

In the first deposited layer right above the substrate displayed in Fig. 12(a) the microstructure consisted of primary acicular martensite α′ with the characteristic of high aspect ratio, as well as a small amount of α lamellae inside the β grains. From the IPF orientation map shown in Fig. 12(b) in this region the primary acicular martensite α′ nucleated at the prior-β grains boundary and grew within the prior-β grain, even penetrating the whole grain. Moreover, the finer secondary α′ was observed clearly between adjacent primary α′, while the finest α/α′ formed among neighbouring secondary α′. However, above the 3rd layer there was almost no acicular α′ formation and the microstructure distributed in the columnar prior-β grains was mostly lathy and plate α with some α lamellae still presented between neighbouring α plates, displayed in Fig. 12(c) and (d). The microstructural formation indicated that with increasing the built layer, the spacing of α/α′ lamellae increased and the martensite α′ was gradually replaced by α lath. In the bottom region, the α/α′ size was distributed in a wide range of 1.8–53.1 μm with an average value of 2.85 μm and average aspect ratio of 1.9. Meanwhile the aspect ratio of α/α′ lath varied from 1 to 47, and the large value represented the acicular α′. The large-angle grain boundaries (HAGBs, ≥ 15°) were predominant over low angle grain boundaries (LAGBs, < 15°). The total fraction of HAGBs within 61 ± 4° and 89.5 ± 1° were 63% and 11% respectively. HAGBs were found to be more desirable as they were better in pinning the dislocations and increasing strength than LAGBs [55].

From the images in Fig. 13(a)–(c), the microstructures in middle region of the sample consisted of boundary α outlining the prior-β grain shape, and short lamella α and fine granular α that interwove with each other instead of the acicular α′ and distributed in the equiaxed or columnar prior-β grain. Hence, it could be observed that the microstructure transferred into basketweave morphology. The coarse and

Fig. 12 Microstructures and EBSD results in bottom region: (**a**) SEM image and (**b**) IPF orientation map in 1st layer; (**c**) SEM image and (**d**) IPF orientation map above 3rd layer
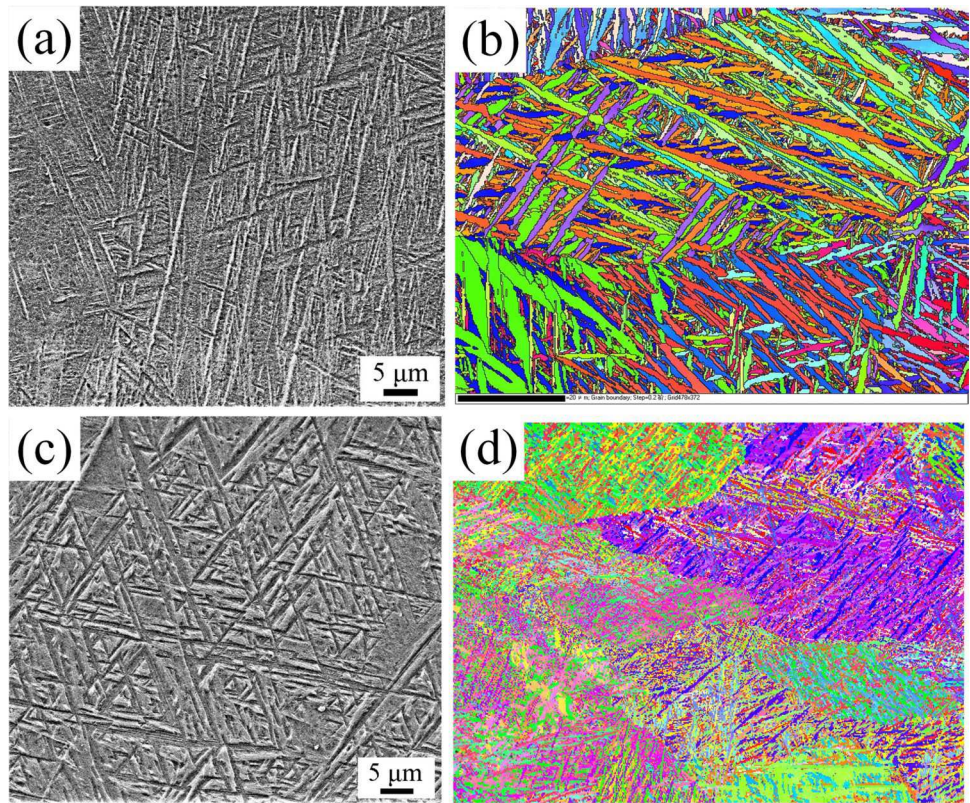
fine basket-weave structures appeared alternately, while the significant decrease in the lamellar length and width was seen compared to bottom region. The phase composition and distribution were similar to those in the bottom region, but there was a significant change in the α size and aspect ratio in comparison. The distribution areas of grain size and aspect ratio shifted to the small values of diameter and aspect ratio compared with the average values at 1.2 μm and 1.4 respectively. The total fraction of HAGBs within $61.5 \pm 4°$ and $89.5 \pm 1°$ were 63% and 16% respectively, indicating similar grain boundary distribution with that in bottom region, except that there was a drift upward in the 89.5° boundary.

Moving towards to the upper region, the basketweave structure of microstructure was maintained, similar in appearance to that in the middle region of the build, but there was an obvious change in α morphology to rod and granular shapes and the α spacing increased as shown in Fig. 14(a). In the last layer of the build as displayed from Fig. 14(b) and (c), the basketweave α structures composed by fine acicular α′ and lamella α generated and distributed in the prior-β grains, attributed to the absence of multiple thermal cycles. Comparison between Fig. 14(a) and (c) indicated there was a drift downwards in the α spacing at the last building layer; meanwhile, the morphology of martensite α′ was similar to that in the initial layer but the length decreased obviously. The coarsening of α rod in the upper region gave rise to the

slight increase of average α/α′ size from 1.2 μm to 1.4 μm, while the average grain aspect ratio also increased to 1.7 due to the presence of long-narrow lath α and martensite α′ in the last layer. In contrast, grain boundary distribution was almost consistent with that of the middle region.

For AM produced Ti-6Al-4 V parts manufactured through different heat sources, line energy densities and AM strategies, the microstructures mainly consist of the acicular α′ with different size scales and α structures with different shapes, transferred from β phase at different cooling rates. Figure 15 depicts the microstructural evolution mechanism in different regions of μLMWD part. It should be noted that during the μLMWD of each layer the microstructure experienced multiple transformations owing to the repeated heating and cooling of the pulsed laser beam. As shown in Fig. 10(a), in the 1st layer while the temperature dropped below $T_β$ during the cooling process after the first laser pulse of thermal cycle 1, the transformation from β to α was inhibited as the fast cooling rate (6050 ℃/s) limited the atomic diffusion. With further cooling below martensite transformation start temperature (M_S), the acicular α′ was obtained by non-diffusive transformation, in which the long primary α′ even penetrating the whole grain formed firstly and then α′ lath with small size came into being between adjacent primary α′ needles, as shown in Fig. 15(a). At later laser pulses the microstructure forming during the previous laser pulses were reheated and transferred into liquid or β phase if the

Fig. 13 Microstructures and EBSD results in middle region: (**a**)-(**c**) SEM images and (**c**) is taken from the rectangle region in (**b**); (**d**) IPF orientation map
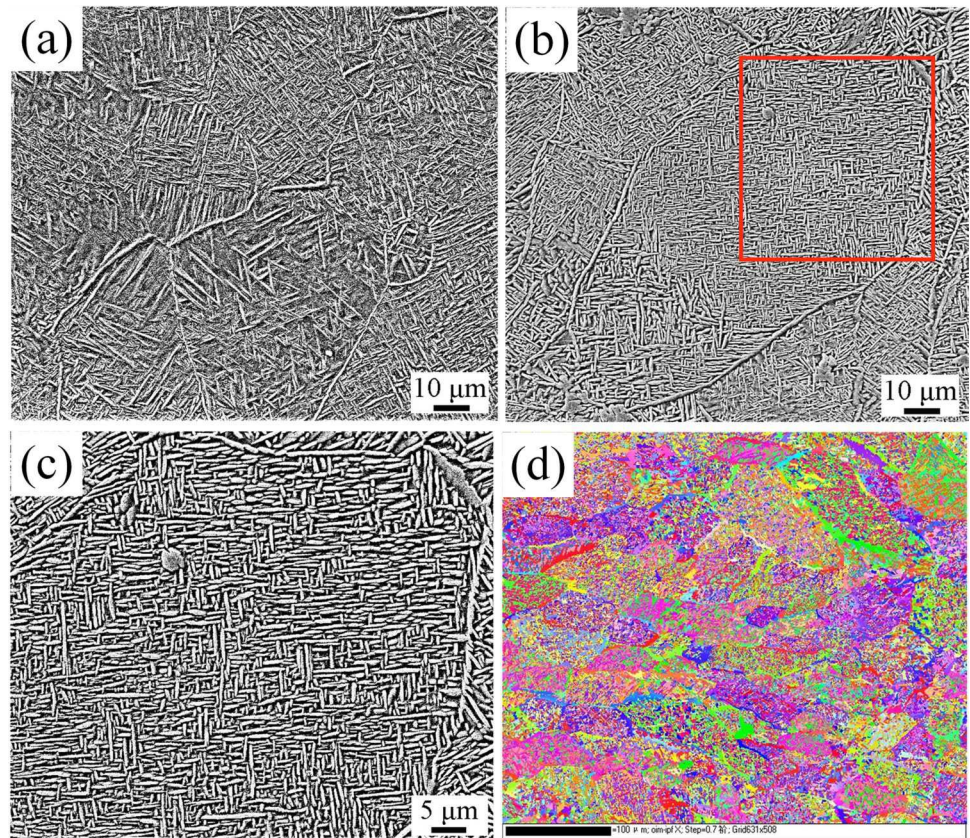

Fig. 14 Microstructures and EBSD results in upper region: (**a**) SEM images in upper region; (**b**) SEM images in last layer; (**c**) is taken from the rectangle region in (**b**)
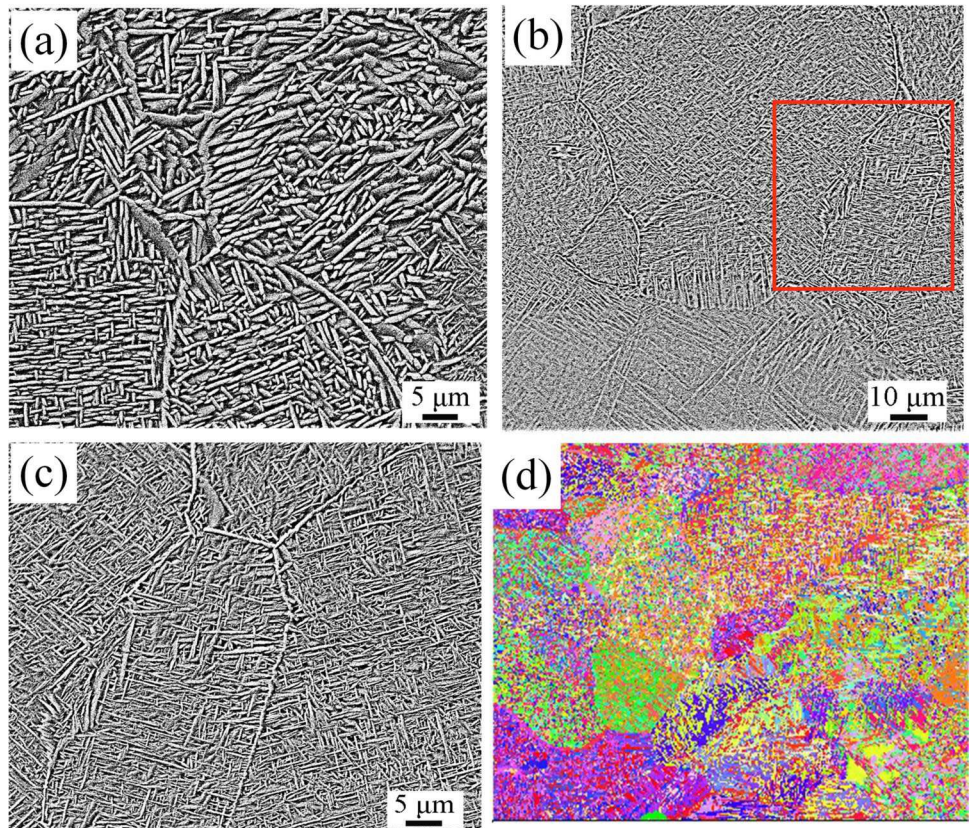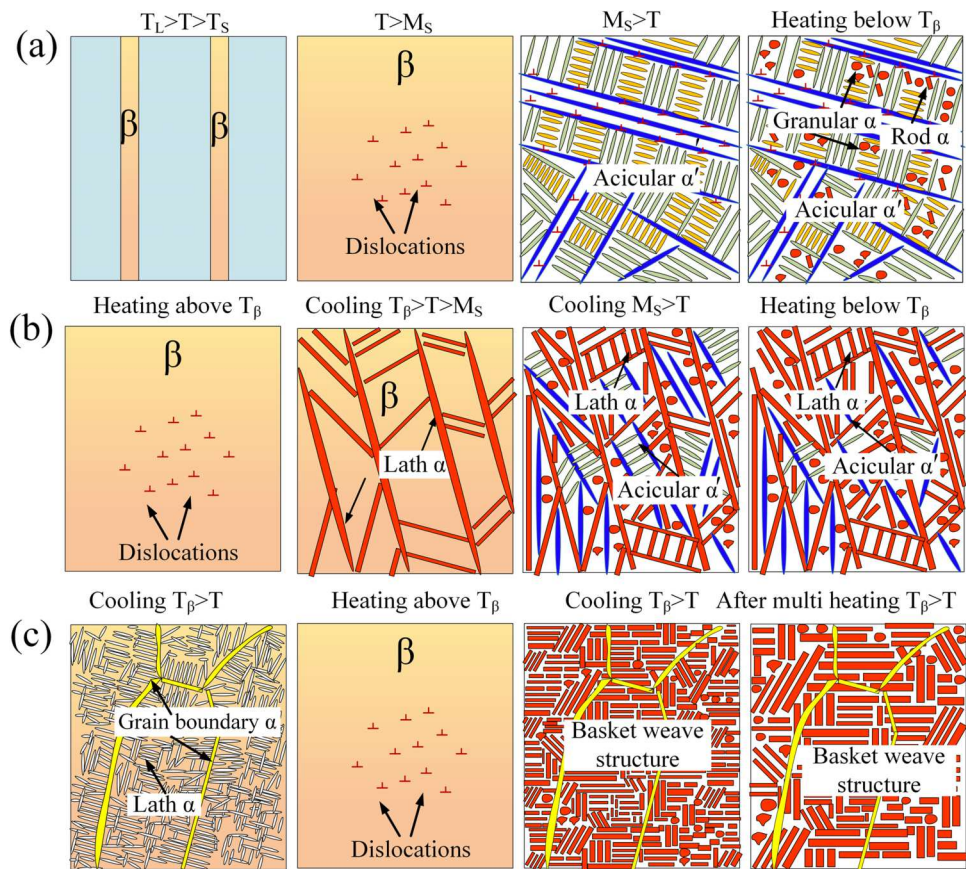
Fig. 15 The diagram illustrating the microstructure transformation mechanism in different regions of μLMWD wall: (**a**) 1st layer; (**b**) 3rd layer; (**c**) middle region

peak temperatures (T_P) exceeded the T_L or T_β, and similar microstructure evolution occurred at subsequent re-cooling process. While new layers were then built, the deposited metal in the 1st layer experienced similar thermal cycles but both the cooling rate and T_P decreased gradually as the laser source was incremented upwards and heat accumulated. At the last thermal cycle whose T_P exceeded T_β, the cooling rate decreased to 800 ℃/s that still far exceeded the critical value (410 ℃/s) to produce martensite. During the laser pulse durations with peak temperatures in the rage of T_β and M_S, a small amount of metastable α′ might be decomposed to α+β structure, regard as a transient heat-treatment process [56, 57]. It could be observed from Fig. 10(b) that the cooling rate at T_β in the first thermal cycles that deposited metal in 3rd layer experiences approached 4150 ℃/s, and thus acicular α′ formed similar to 1st layer. The cooling rate at T_β reduced to 160 ℃/s with the progress of μLMWD, causing α lamella formed by diffusive transformation besides the martensite α′ as displayed in Fig. 15(b). Also, more metastable α′ could be decomposed in the following re-melting and re-solidifying processes.

In middle region with the temperature cooing up to T_β during the thermal cycle 1, α nucleation occurring in the strain field of dislocations within the prior β grain would be promoted owing to the further decrease of cooing rate as

shown in Fig. 10(c), and then more nuclei grew into short α lamella within the strain field which interwove with each other and formed basketweave structure [2]. In contrast, the formation of acicular α′ was limited. Because the deposited metal was heated and cooled repeatedly, the basketweave microstructure would coarsen at gradual decrease cooling rate as shown in Fig. 15(c). Attributed to the absence of long acicular α′ and lath α, there was a significant decrease in the average α/α′ size and grain aspect ratio compared to bottom region. The similar basketweave structure including coarsening lamella and granular α formed in upper region resulting from the lower cooling rate during thermal cycles. However, in the top surface region the microstructure was predominantly short α lamella and acicular α′ constituting basketweave structure due to the absence of thermal cycles.

3.4 Microhardness

Figure 16 displays the microhardness distribution on the cross section of the μLMWD deposited wall, and clear dependence on the wall height could be found. The microhardness in the 1st and 2nd layers of the wall was significantly higher than that in the base metal because of the formation of martensite α′, and by comparison the microhardness from

3rd layer to 5th layer decreased obviously, attributed to the increase of columnar prior-β grain size and the generation of α lath instead of α′. With increasing the deposited layer further, the equiaxed grain formed gradually and the grain refined significantly as mentioned above, bringing more grain boundaries. Besides, there was an obvious decrease of the α size, and the long lath α was replaced by basketweave structure constituting by fine α needles. Consequently, the microhardness increased after 5th deposited layer and then almost remained unchanged in the upper part of the lower region and the whole middle region of the wall. At the top region of the wall, the highest microhardness was obtained, attributed to the small grain size and short α lamella and acicular α′ microstructure because of the absence of multi thermal cycles during the μLMWD process.

4 Conclusions

This work investigated the formability characteristics, grain growth and microstructure evolution during μLMWD of Ti-6Al-4V alloy and succeeded in refining the grain size substantially and promoting the CET in the μLMWD produced wall. The thermal and kinetic sensitive factors affecting the CET and microstructure transformation during μLMWD were explored and the microhardness of the wall was analysed.

(1) The effects of the peak power, pulse duration and gas flow rate of argon on the deposited formability were analyzed and optimized process parameters were obtained by building the fitted regression models and presented the chosen depth and width of the single track. And, the height increment for multi-layer walls was optimized to obtain stable condition during μLMWD process.

(2) Additive manufacturing process was thermally modelled in the initial layer of the wall. The calculated large G/R value is expected to promoted the formation of columnar grain, but the small molten pool size and steep temperature gradient restricted the grain growth, generating columnar grains with smaller grain size in bottom region of the wall compared to those produced in WAAM and LMWD.

(3) In the middle region of the wall, the decrease of G/R ratio tended to provide a condition favouring the formation of equiaxed grain, and nucleant particles are expected to be formed in the mushy zone by the Marangoni force, increasing the curvature radius of nuclei above r* and facilitating their further growth to form equiaxed grains. The CET was promoted and fine equiaxed grains of 45 μm diameter, and short columnar β grains of 62 μm average width and 114 μm average length formed, even finer than those in LPBF manufactured samples. Attributed to the continuous decrease of G and R and the expansion of mushy zone between neighbouring pulse duration, the proportion of equiaxed grains increased in the upper region, and both the equiaxed and columnar grains refined further.

(4) With a pulse duration of 7 ms the calculated cooling rate at $T_β$ varied from 6050 ℃/s to 800 ℃/s at initial layer, generating the acicular α′ by non-diffusive transformation and increased the microhardness. The heat accumulation decreased the cooling rate during μLMWD and hence reduced the acicular α′, decreasing the microhardness in the bottom region of the wall. The short α lamellas formed within the prior β grain due to the continuous decrease of cooing rate, which constituted basketweave structure and coarsened at subsequent thermal cycles. The refined grains and fine basketweave microstructure increased the microhardness significantly. Meanwhile, α lamellas coarsened gradually because of the low cooling rate exceed the top region where multi thermal cycle was absent and highest microhardness was observed.

Fig. 16 The microhardness distribution
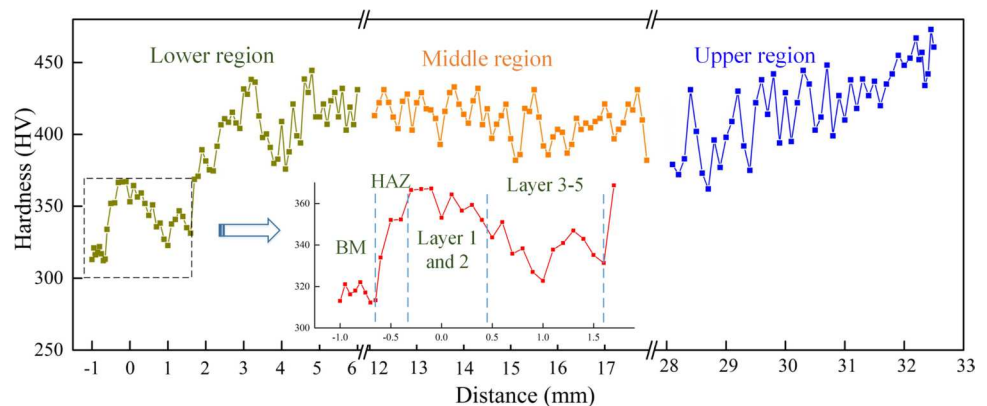
The work underlines that the μLMWD process provides adequate thermal conditions for achieving a highly desirable microstructure for enhanced mechanical properties. However, the geometrical capabilities should be further studied. The use of a similar pulsed wave emission strategy with coaxial wire feeding may allow to improve the geometrical capabilities combined with multiple axes or a robotic manipulator. The use of multiple heads can be beneficial for improved productivity. Considering the lower thermal load applied throughout the μLMWD process compared to the other DED processes, the process stability may be more easily maintained despite the use of multiple heat sources around the built part.

Declarations

Ethics approval Not applicable.

Consent to participate Not applicable.

Consent for publication Not applicable.

Conflict of interest The authors declare no competing interests.

References

1. Baufeld B, Biest OVD, Gault R (2010) Additive manufacturing of Ti-6Al-4V components by shaped metal deposition: microstructure and mechanical properties. Mater Des 31:S106–S111
2. Ho A, Zhao H, Fellowes JW (2019) On the origin of microstructural banding in Ti-6Al-4V wire-arc based high deposition rate additive manufacturing. Acta Mater 166:306–323
3. Wang Z, Beese AM (2017) Effect of chemistry on martensitic phase transformation kinetics and resulting properties of additively manufactured stainless steel. Acta Mater 131:410–422
4. Ford S, Despeisse M (2016) Additive manufacturing and sustainability: an exploratory study of the advantages and challenges. J Clean Prod 137:1573–1587
5. Bermingham MJ, Nicastro L, Kent D, Chen Y, Dargusch MS (2018) Optimising the mechanical properties of Ti-6Al-4V components produced by wire + arc additive manufacturing with post-process heat treatments. J Alloys Compd 753:247–255
6. Tang Q, Pang S, Chen B, Suo H, Zhou J (2014) A three dimensional transient model for heat transfer and fluid flow of weld pool during electron beam freeform fabrication of Ti-6-Al-4-V alloy. Int J Heat Mass Transf 78:203–215
7. Ding D, Pan Z, Cuiuri D, Li H (2015) Wire-feed additive manufacturing of metal components: technologies, developments and future interests. Int J Adv Manuf Technol 81:465–481
8. Nie Z, Wang G, McGuffin-Cawley JD, Narayanan B, Zhang S, Schwam D, Kottman M, Rong Y (2016) Experimental study and modeling of H13 steel deposition using laser hot-wire additive manufacturing. J Mater Process Technol 235:171–186
9. Cai X, Dong B, Yin X, Lin S, Fan C, Yang C (2020) Wire arc additive manufacturing of titanium aluminide alloys using two-wire TOP-TIG welding: processing, microstructures, and mechanical properties. Addit Manuf 35:101344
10. Wen P, Wang G, Chen Y (2017) Effect of laser scanning and powder addition on microstructure and mechanical properties for hot-wire-feed laser additive manufacturing. J Laser Appl 29(2):022302
11. Aalderink BJ, Pathiraj B, Aarts RGKM (2010) Seam gap bridging of laser based processes for the welding of aluminum sheets for industrial applications. Int J Adv Manuf Technol 48(1–4):143–154
12. Yu J, Rombouts M, Maes G, Motmans F (2012) Material properties of Ti6Al4V parts produced by laser metal deposition. Phys Procedia 39:416–424
13. Liu S, Shin YC (2019) Additive manufacturing of Ti6Al4V alloy: a review. Mater Design 164:107552
14. Brandl E, Michailov V, Viehweger B, Leyens C (2011) Deposition of Ti-6Al-4V using laser and wire, part I: microstructural properties of single beads. Surf Coat Technol 206(6):1120–1129
15. Gockel J, Beuth J, Taminger K (2014) Integrated control of solidification microstructure and melt pool dimensions in electron beam wire feed additive manufacturing of Ti-6Al-4V. Addit Manuf 1–4:119–126
16. Syed WU, Pinkerton AJ, Li L (2005) A comparative study of wire feeding and powder feeding in direct diode laser deposition for rapid prototyping. Appl Surf Sci 247(1–4):268–276
17. Abioye TE, Folkes J, Clare AT (2013) A parametric study of Inconel 625 wire laser deposition. J Mater Process Technol 213(12):2145–2151
18. Hussein NIS, Segal J, McCartney DG, Pashby IR (2008) Microstructure formation in Waspaloy multilayer builds following direct metal deposition with laser and wire. Mat Sci Eng A 497(1–2):260–269
19. Huang W, Chen S, Xiao J, Jiang X, Jia Y (2021) Laser wire-feed metal additive manufacturing of the Al alloy. Opt Laser Technol 134:106627
20. Froend M, Bock FE, Riekehr S, Kashaev N, Klusemann B (2018) Experimental investigation of temperature distribution during wire-based laser metal deposition of the Al-Mg alloy 5087. Mater Sci Forum 941:988–994
21. Demir AG (2018) Micro laser metal wire deposition for additive manufacturing of thin-walled structures. Opt Laser Eng 100:9–17
22. Yan C, Liang H, Hussein A, Young P, Raymont D (2014) Advanced lightweight 316L stainless steel cellular lattice structures fabricated via selective laser melting. Mater Des 55:533–541

23. Boyer RR (1996) An overview on the use of titanium in the aerospace industry. Mater Sci Eng A 213(1):103–114

24. Bermingham MJ, StJohn DH, Krynen J, Tedman-Jones S, Dargusch MS (2019) Promoting the columnar to equiaxed transition and grain refinement of titanium alloys during additive manufacturing. Acta Mater 168:261–274

25. Szost BA, Terzi S, Martina F, Boisselier D, Prytuliak A, Pirling T, Hofmann M, Jarvis DJ (2016) A comparative study of additive manufacturing techniques: residual stress and microstructural analysis of CLAD and WAAM printed Ti-6Al-4V components. Mater Des 89:559–567

26. Shi X, Ma S, Liu C, Wu Q, Lu J, Liu Y, Shi W (2017) Selective laser melting-wire arc additive manufacturing hybrid fabrication of Ti-6Al-4V alloy: microstructure and mechanical properties. Mat Sci Eng A 684:196–204

27. Spittle JA (2006) Columnar to equiaxed grain transition in as solidified alloys. Int Mater Rev 51:247–269

28. Xu W, Lui EW, Pateras A, Qian M, Brandt M (2017) In situ tailoring microstructure in additively manufactured Ti-6Al-4V for superior mechanical performance. Acta Mater 125:390–400

29. Fan W, Tan H, Lin X, Huang W (2018) Microstructure formation of Ti-6Al-4 V in synchronous induction assisted laser deposition. Mater Des 160:1096–1105

30. Xue A, Lin X, Wang L, Wang J, Huang W (2019) Influence of trace boron addition on microstructure, tensile properties and their anisotropy of Ti6Al4V fabricated by laser directed energy deposition. Mater Des 181:107943

31. Martina F, Colgrove PA, Williams SW, Meyer J (2015) Microstructure of interpass rolled wire + arc additive manufacturing Ti-6Al-4V components. Metall Mater Trans A 46(12):6103–6118

32. Wang F, Williams SW, Colegrove P, Antonysamy AA (2013) Microstructure and mechanical properties of wire and arc additive manufactured Ti-6Al-4V. Metall Mater Trans A 44(2):968–977

33. Baufeld B, Brandl E, Biest OVD (2011) Wire based additive layer manufacturing: comparison of microstructure and mechanical properties of Ti-6Al-4V components fabricated by laser-beam deposition and shaped metal deposition. J Mater Process Technol 211:1146–1158

34. Yang J, Yu H, Yin J, Gao M, Wang Z, Zeng X (2016) Formation and control of martensite in Ti-6Al-4V alloy produced by selective laser melting. Mater Des 108:308–318

35. Fu Y, Guo N, Wang G, Yu M, Cheng Q, Zhang D (2021) Underwater additive manufacturing of Ti-6Al-4V alloy by laser metal deposition: formability, gran growth and microstructure evolution. Mater Des 197:109196

36. Capello E, Colombo D, Previtali B (2005) Repairing of sintered tools using laser cladding by wire. J Mater Process Technol 164:990–1000

37. Capello E, Previtali B (2006) The influence of operator skills, process parameters and materials on clad shape in repair using laser cladding by wire. J Mater Process Technol 174:223–232

38. Ascari A, Fortunato A, Lutey AH, Guerrini G, Pagano N (2016) Long pulse laser wire deposition of hard steels. Phys Procedia 83:723–732

39. Shaikh MO, Chen CC, Chiang HC, Chen JR, Chuang CH (2019) Additive manufacturing using fine wire-based laser metal deposition. Rapid Prototyp J 26:473–483

40. Demir AG, Biffi CA (2019) Micro laser metal wire deposition of thin-walled Al alloy components: process and material characterization. J Manuf Process 37:362–369

41. Kobryn PA, Semiatin SL (2003) Microstructure and texture evolution during solidification processing of Ti-6Al-4V. J Mater Process Technol 135:330–339

42. Zhan XH, Liu Y, Ou WM, Gu C, Wei YH (2015) The numerical and experimental investigation of the multi-layer laser-MIG hybrid welding for Fe36Ni invar alloy. J Mater Eng Perform 24:4948–4957

43. Panwisawas C, Perumal B, Ward RM, Turner N, Turner RP, Brooks JW, Basoalto HC (2017) Keyhole formation and thermal fluid flow-induced porosity during laser fusion welding in titanium alloys: experimental and modelling. Acta Mater 126:251–263

44. Mills KC (2002) Recommended values of thermophysical properties for selected commercial alloys. Woodhead Publishing Ltd, England

45. Bontha S, Klingbeil NW, Kobryn PA, Fraser HL (2009) Effects of process variables and size-scale on solidification microstructure in beam-based fabrication of bulky 3D structures. Mater Sci Eng A 513–514:311–318

46. Carroll BE, Palmer TA, Beese AM (2015) Anisotropic tensile behavior of Ti-6Al-4V components fabricated with directed energy deposition additive manufacturing. Acta Mater 87:309–320

47. DebRoy T, Wei HL, Zuback JS, Mukherjee T, Elmer JW, Milewski JO, Beese AM, Wilson-Heid A, De A, Zhang W (2018) Additive manufacturing of metallic components - process, structure and properties. Prog Mater Sci 92:112–224

48. Brandl E, Schoberth A, Leyens C (2012) Morphology, microstructure, and hardness of titanium (Ti-6Al-4V) blocks deposited by wire-feed additive layer manufacturing (ALM). Mater Sci Eng A 532:295–307

49. Kashaev N, Ventzke V, Fomichev V, Fomin F, Riekehr S (2016) Effect of Nd:YAG laser beam welding on weld morphology and mechanical properties of Ti-6Al-4V butt joints and T-joints. Opt Laser Eng 86:172–180

50. Karimzadeh F, Ebnonnasir A, Foroughi A (2006) Artificial neural network modeling for evaluating of epitaxial growth of Ti6Al4V weldment. Mater Sci Eng A 432:184–190

51. Jiang M, Li BC, Chen X, Tan CW, Lei ZL, Zhao SC, Chen YB (2022) Numerical study of thermal fluid dynamics and solidification characteristics during continuous wave and pulsed wave laser welding. Int J Therm Sci 181:107778

52. Cai YH, Luo Y, Zhang FY, Peng YR, Yang SQ, Tang FS (2023) Effect of pulsed laser energy on grain morphology and texture characteristics of stainless steel fabricated by laser-PTA additive manufacturing. Opt Laser Technol 158:108799

53. Greer AL, Cooper PS, Meredith MW, Schnider W, Schumacher P, Spittle JA, Tronche A (2003) Grain refinement of aluminium alloys by inoculation. Adv Eng Mater 5:81–91

54. Greer AL, Bunn AM, Tronche A, Evans PV, Bristow DJ (2000) Modelling of inoculation of metallic melts: application to grain refinement of aluminium by Al-Ti-B. Acta Mater 48:2823–2835

55. Chen SJ, Yu Q (2019) The role of low angle grain boundary in deformation of titanium and its size effect. Scripta Mater 163:148–151

56. Wysocki B, Maj P, Sitek R, Buhagiar J, Kurzydłowski K, Święszkowski W (2017) Laser and electron beam additive manufacturing methods of fabricating titanium bone implants. Appl Sci 7(7):657

57. Galarraga H, Lados DA, Dehoff RR, Kirka MM, Nandwana P (2016) Effects of the micro- structure and porosity on properties of Ti-6Al-4V ELI alloy fabricated by electron beam melting (EBM). Addit Manuf 10:47–57